Incorporation of Li into MnOOH: An In Situ X-ray and Neutron Diffraction Study

Gareth R. Williams,[†] Alexander J. Norquist,[‡] and Dermot O'Hare*,[†]

Chemistry Research Laboratory, Department of Chemistry, University of Oxford, Mansfield Road, Oxford OX1 3TA, United Kingdom, and Department of Chemistry, Haverford College, 370 Lancaster Avenue, Haverford, Pennsylvania 19041

Received May 19, 2006

In situ X-ray and neutron diffraction techniques were used to study the synthesis of $LiMnO_2$ from γ-MnOOH and LiOH under mild hydrothermal conditions. These complementary techniques allow for both good time (X-rays) and good peak (neutrons) resolution. After a significant induction period, the formation of $LiMnO_2$ occurs rapidly and without transient intermediates. The Avrami−Erofe'ev model has been used to deduce the reaction mechanism, which is believed to involve shearing of vertex links in the MnOOH starting material and the condensation of chains into layers. The mechanism involves deceleratory nucleation and 1D propagation of the layers perpendicular to the layer planes. The activation energy is 81.2 kJ mol^{-1} for the reaction between LiOH and MnOOH and 150.2 kJ mol^{-1} for the LiOD/MnOOD reaction. These values are consistent with nucleation control: the difference between the two values is ascribed to the kinetic isotope effect.

Introduction

As the demand for electronic goods increases, energy sources are continually required to be smaller and deliver more power. In addition, the environmental impact associated with new technologies has driven developments in "green" technologies. Previous generations of battery materials have involved the use of single-use components that are highly toxic (e.g., NiCd batteries); this technology is clearly not sustainable long term, and current and future developments have moved toward reusable and environmentally friendly systems.

Rechargeable Li battery technology has already enjoyed tremendous success in the electronics industry.[1,2] These devices are capable of providing in excess of 3 times more energy per unit weight and volume than conventional batteries. The first commercial Li cell (produced by Sony) employed $LiCoO_2$ as the cathode and powdered graphite as the anode. Unfortunately, this contains expensive and toxic components and is unable to supply sufficient energy for either static energy storage or hybrid energy vehicles.[3]

Spinel-type lithium manganese oxides, $Li_xMn_2O_4$,[4] which meet cost, toxicology, and efficiency criteria, have been investigated extensively as possible intercalation hosts.[5] However, problems exist with the reproducible synthesis and lifetimes of such materials, owing to the possibility of structural changes during the charging and discharging cycles. $LiMn_2O_4$, which has received significant attention, is found to cycle poorly and to have energy storage values of 110−120 mAh g^{-1}, well short of the theoretical limits for this material, 148 mAh g^{-1}. As a result of these deficiencies, $LiMnO_2$[6] has begun to be investigated as a replacement, owing to a high theoretical capacity of 285 mAh g^{-1}.[7,8]

Two polymorphs of $LiMnO_2$ exist: an orthorhombic form and a monoclinic modification,[9,10] with the former being more stable than the latter.[11,12] A number of synthesis methods for $LiMnO_2$ are known, usually requiring temperatures of ca. 1000 °C.[13−18] A synthesis using γ-MnOOH[19] and LiOH at ca. 400 °C was reported by Reimers and coworkers, who later found that these reagents can be used to produce $LiMnO_2$ through ion exchange at 100 °C.[20] Duan et al. have developed this synthesis to produce a phase-pure

* To whom correspondence should be addressed. E-mail: dermot.ohare@chem.ox.ac.uk.
[†] University of Oxford.
[‡] Haverford College.

(1) Bruce, P. G. *Chem. Commun.* **1997**, 1817.
(2) Nagaura, T.; Tazawa, K. *Prog. Batteries Sol. Cells* **1990**, *9*, 20.
(3) Bruce, P. G. *Solid State Sci.* **2005**, *7*, 1456.
(4) Mosbah, A.; Verbaere, A.; Tournoux, M. *Mater. Res. Bull.* **1983**, *18*, 1375.
(5) Chung, K. Y.; Kim, K. B. *Electrochim. Acta* **2004**, *49*, 3327.
(6) Hoppe, R.; Brachtel, G.; Jansen, M. *Z. Anorg Allg. Chem.* **1975**, *417*, 1.
(7) Ammundsen, B.; Paulsen, J. *Adv. Mater.* **2001**, *13*, 943.
(8) Bruce, P. G.; Armstrong, A. R.; Gitzendanner, R. L. *J. Mater. Chem.* **1999**, *9*, 193.
(9) Chiang, Y. M.; Wang, H. F.; Jang, Y. I. *Chem. Mater.* **2001**, *13*, 53.
(10) Jang, Y. I.; Chiang, Y. M. *Solid State Ionics* **2000**, *130*, 53.
(11) Jang, Y. I.; Moorehead, W. D.; Chiang, Y. M. *Solid State Ionics* **2002**, *149*, 201.
(12) Mackrodt, W. C.; Williamson, E. A.; Williams, D.; Allan, N. L. *Philos. Mag. B* **1998**, *77*, 1077.
(13) Armstrong, A. R.; Bruce, P. G. *Nature* **1996**, *381*, 499.
(14) Bach, S.; Henry, M.; Baffier, N.; Livage, J. *J. Solid State Chem.* **1990**, *88*, 325.
(15) Davidson, I. J.; McMillan, R. S.; Murray, J. J.; Greedan, J. E. *J. Power Sources* **1995**, *54*, 232.
(16) Guo, Z. P.; Wang, G. X.; Konstantinov, K.; Liu, H. K.; Dou, S. X. *J. Alloys Compd.* **2002**, *346*, 255.
(17) Katayama, K.; Kamiyama, H. *Key Eng. Mater.* **1999**, *157−158*, 281.
(18) Lee, Y. S.; Sun, Y. K.; Adachi, K.; Yoshio, M. *Electrochim. Acta* **2003**, *48*, 1031.
(19) Buerger, M. J. *Z. Kristallogr., Kristallgeom., Kristallphys., Kristallchem.* **1936**, *95*, 163.

10.1021/cm0611791 CCC: $33.50
Published on Web 07/18/2006

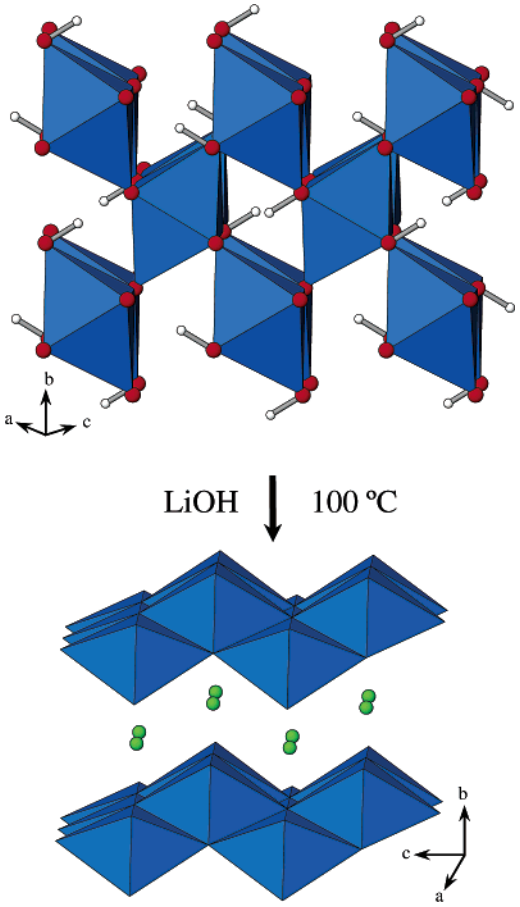

Figure 1. Schematic showing the conversion of γ-MnOOH to the orthorhombic form of $LiMnO_2$ through reaction with LiOH. MnO_6 octahedra are shown in blue, and O, H, and Li^+ are shown as red, white, and green spheres, respectively.

orthorhombic form of $LiMnO_2$ with good electrochemical properties, an initial discharge capacity of 220 mAh g^{-1}, and a reversible capacity of 194 mAh g^{-1} after 30 cycles.[21] See Figure 1. Despite the great potential of $LiMnO_2$, almost nothing is known about the transformation from MnOOH to $LiMnO_2$.

In this paper, a detailed kinetic and mechanistic study into the formation of orthorhombic $LiMnO_2$ from γ-MnOOH is reported. A combined in situ X-ray and neutron diffraction study was performed. In situ diffraction is a powerful technique for monitoring solid-state reaction processes. The use of high-intensity X-rays and an energy-discriminating detector allows the simultaneous collection of data from 0.2 to 16 Å in less than 1 min.[22] Reflections corresponding to the starting material, any intermediate phases, and the product can be observed at the same time. Therefore, the evolution in intensity of characteristic peaks can be reliably monitored as a function of time, allowing mechanistic and kinetic parameters to be determined. The same is true for in situ neutron diffraction; by using the high-energy, high-intensity detector on the General Materials (GEM) diffractometer at the ISIS neutron source at the Rutherford Appleton Laboratory, Rietveld-quality diffraction patterns can be collected in as little as 5 min.[19] In situ neutron diffraction (ND)[23] is particularly useful for the study of the MnOOH/$LiMnO_2$ system, allowing the resolution of reflections other than the most intense and peaks at similar *d* spacings. The detectors used for energy-dispersive X-ray diffraction (EDXRD) have poor resolution, and therefore, it is difficult to distinguish weak reflections and those with similar *d* spacings. In contrast, these reflections may be easily resolved using ND. In situ EDXRD and ND have previously been used to investigate a variety of reactions.[24−32]

Experimental Section

Starting Materials. MnOOH was synthesized by combining 2.55 g of $MnSO_4$ (BDH, 97%) with 5 mL of a H_2O_2 solution (35 wt % in water, Aldrich) and 250 mL of deionized H_2O. A separate solution of 3 mL of a NH_4OH solution (Aldrich, 5 M, 28 wt %) and 72 mL of H_2O was prepared. The two solutions were combined and then refluxed at 100 °C for 24 h. The resulting precipitate was characterized by X-ray powder diffraction, IR spectroscopy, and elemental analysis. MnOOD (for ND experiments) was synthesized in an analogous fashion, but using D_2O and NaOD as appropriate, owing to incoherent scattering by H in neutron diffraction experiments. A 9 wt % LiOH solution was prepared from LiOH (98%, Aldrich) and deionized H_2O. LiOD was supplied as a 9 wt % solution in D_2O by Aldrich.

Time-Resolved in Situ Energy-Dispersive X-ray Diffraction. Experiments were carried out on Station 16.4 of the U.K. Synchrotron Radiation Source (SRS) at the Daresbury Laboratory. The SRS operates with an average stored current of 200 mA and a typical beam energy of 2 GeV. A wiggler working at a peak field of 6 T supplies Station 16.4 with X-ray frequency radiation. The usable X-ray flux is continuous in the range 5−120 keV, with a maximum flux of 3×10^{10} photons s^{-1} at approximately 13 keV. A three-element detector system is employed.[33] Each detector is separated by approximately 2° in 2θ and covers a different range of *d* spacings. Detectors are fixed during a given experiment, but can be adjusted between runs.

Reactions were performed in Teflon-lined stainless steel autoclaves that were contained within a temperature-controlled block (Figure 2), the details of which have been discussed elsewhere.[34,35]

(20) Reimers, J. N.; Fuller, E. W.; Rossen, E.; Dahn, J. R. *J. Electrochem. Soc.* **1993**, *48*, 1031.
(21) Li, X.-D.; Yang, W.-S.; Zhang, S.-C.; Evans, D. G.; Duan, X. *Solid State Ionics* **2005**, *176*, 803.
(22) Evans, J. S. O.; Francis, R. J.; Price, S. J.; Clark, S. M.; Flaherty, J.; Gordon, J.; Nield, A.; Tang, C. C. *Rev. Sci. Instrum.* **1995**, *66*, 2442.
(23) Walton, R. I.; Francis, R. J.; Halasyamani, P. S.; O'Hare, D.; Smith, R. I.; Done, R.; Humphreys, R. J. *Rev. Sci. Instrum.* **1999**, *70*, 3391.
(24) Fogg, A. M.; Price, S. J.; Francis, R. J.; O'Brien, S.; O'Hare, D. *J. Mater. Chem.* **2000**, *10*, 2355.
(25) Loh, J. S. C.; Fogg, A. M.; Watling, H. R.; Parkinson, D. M.; O'Hare, D. *Phys. Chem. Chem. Phys* **2000**, *2*, 3597.
(26) Millange, F.; Walton, R. I.; O'Hare, D. *J. Mater. Chem.* **2000**, *10*, 1713.
(27) Walton, R. I.; O'Hare, D. *Chem. Commun.* **2000**, 2283.
(28) Walton, R. I.; Smith, R. I.; O'Hare, D. *Microporous Mesoporous Mater.* **2001**, *48*, 79.
(29) Walton, R. I.; Norquist, A. J.; Neeraj, S.; Natarajan, S.; Rao, C. N. R.; O'Hare, D. *Chem. Commun.* **2001**, 1990.
(30) Williams, G. R.; Khan, A. I.; O'Hare, D. *Struct. Bonding* **2006**, *119*, 161.
(31) Norquist, A. J.; O'Hare, D. *J. Am. Chem. Soc.* **2004**, *126*, 6673.
(32) Geselbracht, M. J.; Noailles, L. D.; Ngo, L. T.; Pikul, J. H.; Walton, R. I.; Cowell, E. S.; Millange, F.; O'Hare, D. *Chem. Mater.* **2004**, *16*, 1153.
(33) Muncaster, G.; Davies, A. T.; Sankar, G.; Catlow, C. R. A.; Thomas, J. M.; Colston, S. L.; Barnes, P.; Walton, R. I.; O'Hare, D. *Phys. Chem. Chem. Phys.* **2000**, *2*, 3523.
(34) Clark, S. M.; Nield, A.; Rathbone, T.; Flaherty, J.; Tang, C. C.; Evans, J. S. O.; Francis, R. J.; O'Hare, D. *Nucl. Instrum. Methods Phys. Res., Sect. B* **1995**, *97*, 98.

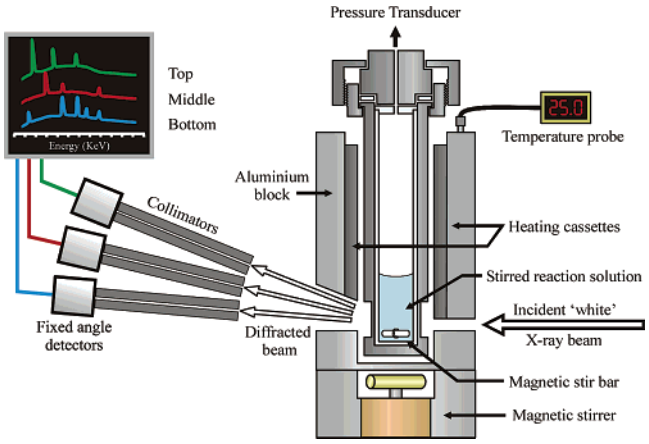

Figure 2. Apparatus used to monitor hydrothermal processes using EDXRD.

The reaction suspension was stirred to ensure a constant amount of sample was always present in the beam. EDXRD spectra were collected at a detector angle of ca. 2° in 2θ,[28] with an acquisition time of 60 s.

Time-Resolved in Situ Neutron Diffraction. Time-resolved ND experiments were performed on the GEM diffractometer at the ISIS neutron source at Chilton, U.K. GEM is a very-high-flux, medium-resolution to high-resolution time-of-flight diffractometer, which allows the rapid collection of data (scans can be as short as 5 min) on relatively small sample sizes. It has six detector banks placed at fixed angles around the sample. In situ neutron diffraction experiments were carried out using the Oxford-ISIS hydrothermal cell,[36] which consists of a temperature-controlled gold-lined ZrTi autoclave equipped with an electronic stirrer to ensure that there is a constant concentration of sample in the beam. Data were recorded with a scan length of 5−10 min. Reactions conducted at 80 °C used 10 min scans, while reactions at 90 °C or above used 5 min scans. The increased time scale for data collection with ND required lower temperatures to be used to monitor the reactions successfully.

In Situ Experimental Details. For both EDXRD and ND, reactions were performed as follows. A 0.5 g sample of MnOOH (EDXRD) or MnOOD (ND) was weighed out into the reaction vessel, to which 6 mL of H_2O (D_2O) and 4 mL of a 9 wt % solution of LiOH (LiOD) were added at room temperature. The reaction vessel was sealed and subsequently transferred to the sample stage. In the case of EDXRD, the sealed vessel was transferred to a preheated sample stage to minimize the time required for the reaction to reach the appropriate temperature, and data collection began within 2 min. The ND experiments require evacuation of the instrument chamber, which takes approximately 5 min. An initial scan was recorded at room temperature, followed by a rapid heating to the desired temperature that required approximately 5−10 min. This delay neither affects the reaction nor influences the calculated parameters from the collected data because the reaction is extremely slow at room temperature and the induction times observed in the EDXRD experiments are longer than any heating delay time. Diffraction patterns were collected until all the observed reflections had attained a constant intensity. The reaction vessel was then cooled to room temperature and opened and the sample suspension retrieved. The products were filtered, dried, and characterized using X-ray powder diffraction (XRD) to ensure that the reaction was complete.

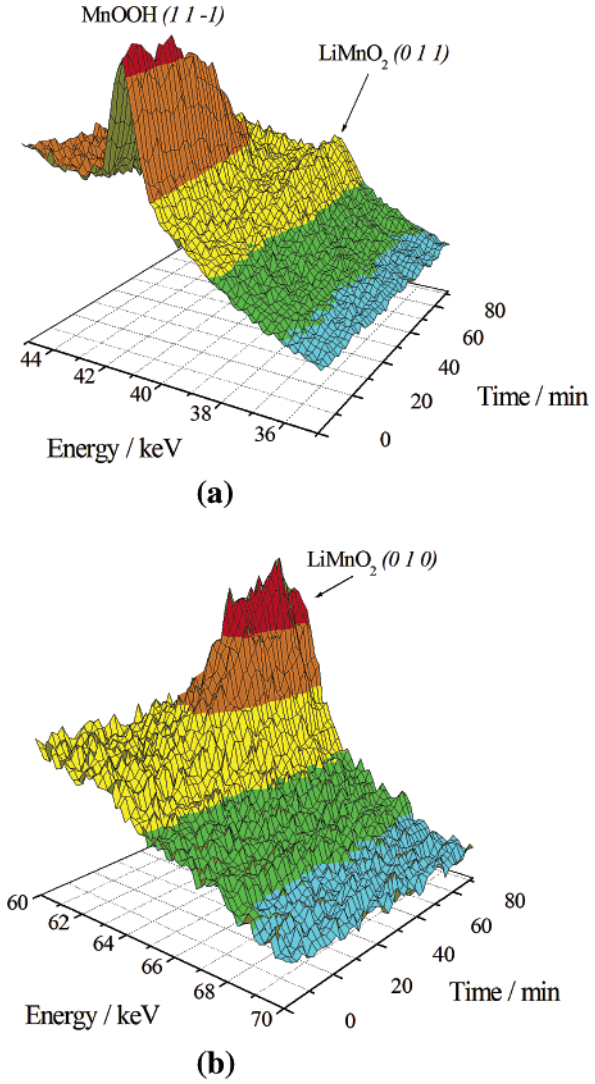

Figure 3. 3D stacked plots showing the EDXRD data for the reaction between MnOOH and LiOH at 100 °C. The decline in intensity of the (1 1 −1) reflection of MnOOH and growth of the (0 1 1) and (0 1 0) reflections of $LiMnO_2$ are clearly visible. Data from the middle and bottom detectors are depicted in **(**a) and (b**),** respectively.

Data Analysis. An automated Gaussian fitting routine is used to obtain the peak areas of the Bragg reflections, which are converted to the extent of reaction at time t, $\alpha(t)$, defined as $\alpha(t) = I_{hkl}(t)/I_{hkl}(\max)$, where $I_{hkl}(t)$ is the area of a given peak at time t and $I_{hkl}(\max)$ is the maximum area of this peak. The intercalation processes were modeled using the Avrami−Erofe'ev model.[37−40] This is the most commonly employed approach for describing solid-state reaction processes. This rate law has been derived in a number of ways, indicating its general applicability and validity. The equation takes the form

$$[-[\ln(1-\alpha)]]^{1/n} = k(t - t_0) \qquad (1)$$

where t_0 is the induction time for the reaction. This expression has been successfully applied to a number of solid-state processes, including phase transformations,[41] decompositions,[42] and crystal-

(35) Evans, J. S. O.; Francis, R. J.; O'Hare, D.; Price, S. J.; Flaherty, J.; Gordon, A.; Nield, A.; Tang, C. C. *Rev. Sci. Instrum.* **1995**, *66*, 2442.
(36) Walton, R. I.; Francis, R. J.; Halasyamani, P. S.; O'Hare, D. *Rev. Sci. Instrum.* **1999**, *70*, 3391.
(37) Avrami, M. *J. Chem. Phys.* **1939**, *7*, 1103.
(38) Avrami, M. *J. Chem. Phys.* **1940**, *8*, 212.
(39) Avrami, M. *J. Chem. Phys.* **1941**, *9*, 177.
(40) Erofe'ev, B. V. *Dokl. Acad. Sci. USSR* **1946**, *52*, 511.
(41) Sheridan, A. K.; Anwar, J. *Chem. Mater.* **1996**, *8*, 1042.
(42) Hancock, J. D.; Sharp, J. H. *J. Am. Ceram. Soc.* **1972**, *55*, 74.

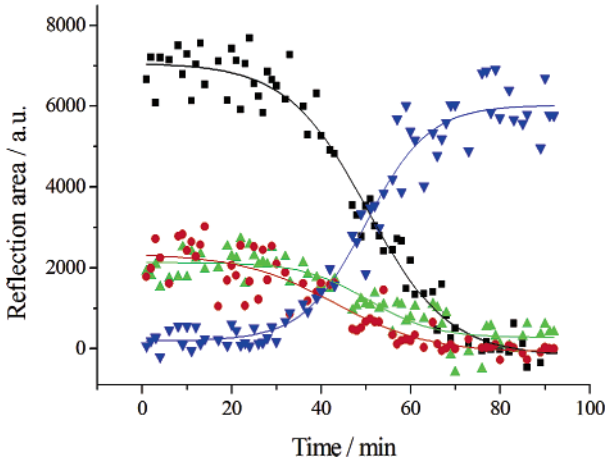

Figure 4. 2D plot showing the decline in intensity with time of the MnOOH (1 1 −1) (black squares), (1 0 2/2 0 0) (red circles), and (1 1 1) (green triangles) reflections and the growth of the $LiMnO_2$ (0 1 0) reflection (blue inverted triangles) at 100 °C, as measured using EDXRD. The solid lines are a guide for the eye only and have no physical significance.

lization and intercalation reactions.[43,44] The equation is found to fit most closely with the experimental data within the range $0.15 < \alpha < 0.85$. Sharp−Hancock plots, $\ln[-[\ln(1-\alpha)]]$ vs ln(time), give straight lines of gradient n and intercept $n \ln k$. The value of n can be used to elucidate reaction mechanisms. These interpretations are based upon the work of Hulbert, who analyzed calculated values of n in a series of "ideal" reactions.[45]

Results

EDXRD Experiments. The incorporation of Li into MnOOH was successfully monitored over the temperature range 93−130 °C. A 3D stacked plot illustrating the time evolution of the starting material and product reflections at 100 °C is presented in Figure 3. The intensities of reflections corresponding to MnOOH are observed to decline smoothly, following an induction time. Concomitant with this, reflections attributable to $LiMnO_2$ begin to appear in the diffraction pattern. This is additionally observed in plots of the integrated intensity vs time (Figure 4), in which multiple reflections corresponding to MnOOH can be clearly resolved.

The temperature at which the reaction is performed has a profound effect on the growth and decay curves obtained experimentally for the products and starting materials, respectively. Plots of the normalized intensity (α) vs time for the MnOOH (1 1 −1) and $LiMnO_2$ (0 1 0) reflections at different temperatures are given in parts (a) and (b), respectively, of Figure 5. In all cases, a significant induction time is seen before the reaction begins.

Sharp−Hancock plots of $\ln[-[\ln(1-\alpha)]]$ vs $t - t_0$ for the $LiMnO_2$ (0 1 0) reflection have been generated to determine the values of the Avrami exponent, n, and the rate constant, k, at different temperatures. These are included in Figure 6. The kinetic parameters calculated from the Sharp-Hancock plots are summarized in Table 1. The reaction at 130 °C was found to be too rapid to calculate accurate values

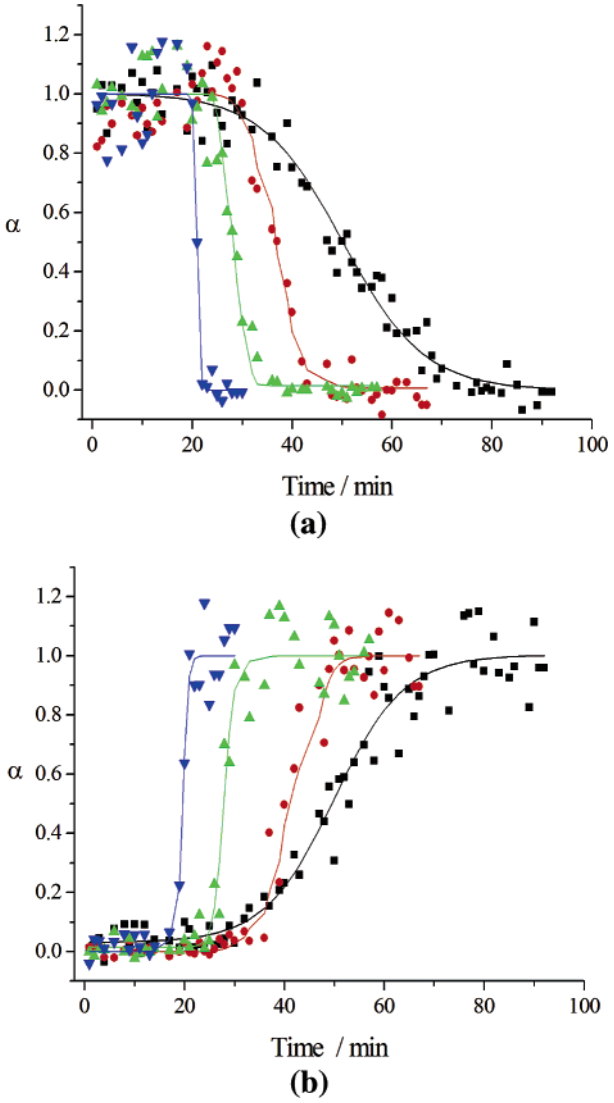

Figure 5. Extent of reaction vs time plots for the **(**a**)** MnOOH (1 1 −1) and **(b)** $LiMnO_2$ (0,1,0) reflections at 100 (black squares), 110 (red circles), 120 (green triangles), and 130 (blue inverted triangles) °C. Data at 93 °C have been omitted for clarity. The solid lines are a guide for the eye only and have no physical significance.

for n and k; however, reasonable values for the induction time and reaction half-life could be obtained and are contained in Table 1. The exponent n provides information on the reaction mechanism, and the rate constants allow the calculation of the activation energy via the Arrhenius relationship. First, it is instructive to consider the form of the extent of reaction curves of both the MnOOH starting material and the $LiMnO_2$ product. In all cases, it is observed that the extent of reaction vs time curves of MnOOH and $LiMnO_2$ cross very close to $\alpha = 0.5$ (see Figure 7). This is indicative that the reaction is a direct transformation: no intermediate phases are present on the reaction coordinate.

The Avrami exponent n is found to lie between 1 and 2, which corresponds to either 1D phase boundary control following deceleratory nucleation or 2D diffusion control following deceleratory nucleation. From the in situ EDXRD data alone, it is not possible to distinguish between these possibilities. However, more insight into the mechanism can be obtained from a consideration of the structural changes occurring during reaction.

(43) Price, S. J.; Evans, J. S. O.; Francis, R. J.; O'Hare, D. *Adv. Mater.* **1996**, *8*, 582.
(44) Wilkinson, A. P.; Speck, J. S.; Cheetham, A. J.; Natarajan, S.; Thomas, J. M. *Chem. Mater.* **1994**, *6*, 750.
(45) Hulbert, S. F. *J. Br. Ceram. Soc.* **1969**, *6*, 11.

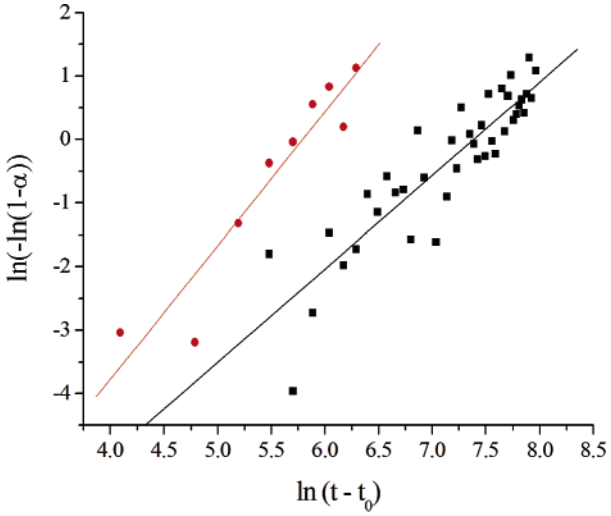

Figure 6. Sharp−Hancock plots for the $LiMnO_2$ reflection at 93 (black squares) and 110 (red circles) °C. Data at 100 and 120 °C have been omitted for clarity.

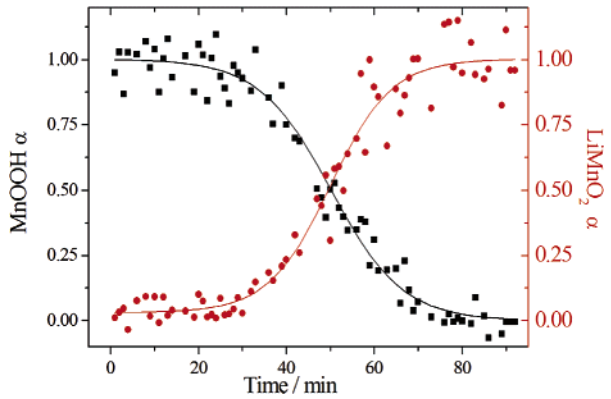

Figure 7. Extent of reaction vs time plots for the reaction of LiOH and MnOOH at 100 °C, showing the direct conversion of the starting material to the product. The solid lines are a guide for the eye only and have no physical significance.

Table 1. Kinetic Parameters for the Formation of $LiMnO_2$ from MnOOH and LiOH, Calculated from EDXRD Data

T/°C	*n*	$k/(10^{-4}\ s^{-1})$	t_0/s	$t_{0.5}$/s
93	1.47 ± 0.12	6.20 ± 1.35	4740	6000
100	1.30 ± 0.09	7.35 ± 1.72	1860	2980
110	2.11 ± 0.27	16.2 ± 3.89	1620	2010
120	2.00 ± 0.31	34.0 ± 4.40	1260	1430
130			720	880

The MnOOH structure consists of 1D chains of MnO_6 octahedra sharing two opposite equatorial edges. Additional equatorial and axial vertexes within each chain are then shared with adjacent chains, forming a 3D structure. Oxide and hydroxides alternate within the structure. The $LiMnO_2$ structure is 2D, with Li^+ cations lying between MnO_2^- layers. The layers are made up of chains of edge-sharing MnO_6 octahedra. Each octahedron in the chain then shares a further two edges with each of two adjacent chains, to form double layers of MnO_6 octahedra (Figure 1). The "nucleation sites" for this reaction consist of the regions of the MnOOH particles where the reaction is initiated. The transformation from MnOOH to $LiMnO_2$ involves the shearing of two of the corner linkages between chains in MnOOH and the condensation of the edge-linked MnO_6 chains to form double layers (see Figure 8).

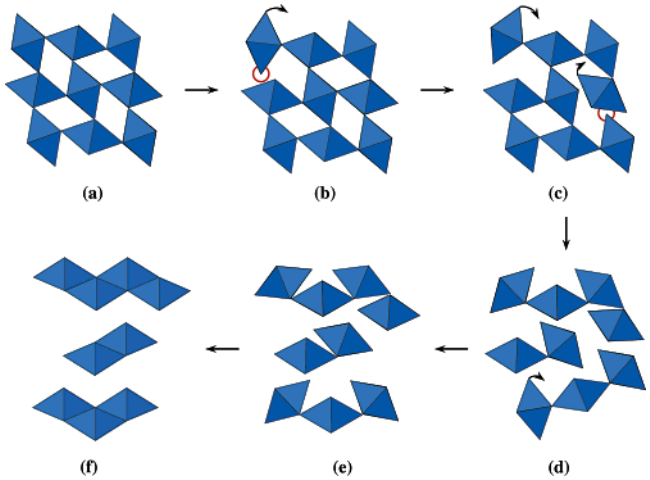

Figure 8. Proposed mechanism for the conversion of MnOOH into $LiMnO_2$ upon reaction with LiOH. In **(**a**)** the MnOOH material, containing vertex-linked chains of MnO_6 octahedra, is illustrated. In **(**b**)** the first nucleation event is depicted: one of the corner linkages is broken. This induces strain into the structure and promotes further linkage breakages in the vicinity of the first fission, as shown in **(**c) and (d**)**. In **(e)** sufficient vertex joints have been broken that the layered nature of the product material can be observed. The linked chains begin to come together and condense to share edges, producing the MnO_2^- layers depicted in **(**f**)**. The blue polyhedra represent MnO_6 octahedra; Li and H atoms are omitted for clarity. Red circles highlight the sites where vertex links have been broken, and the arrows represent the movement of the chains.

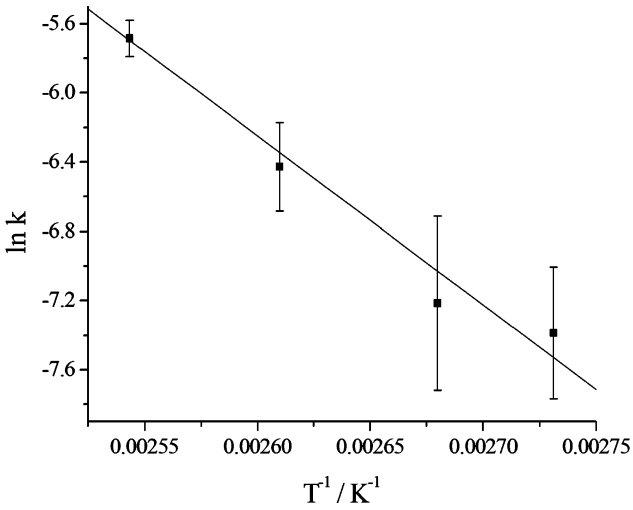

Figure 9. An Arrhenius plot for the reaction of LiOH with MnOOH.

The Arrhenius equation may be used to calculate a value for the activation energy. A plot of ln *k* vs 1/*T* is included in Figure 9. This gives $E_a = 81.2 \pm 6.6$ kJ mol^{-1}, consistent with a nucleation-controlled process.

ND Experiments. The higher resolution of the detectors on the GEM diffractometer allowed resolution of Bragg reflections that could not be satisfactorily observed using EDXRD, particularly those with very similar *d* spacings (see Figure 10b). Sample data are given in Figure 10. Again, a direct transformation between MnOOH and $LiMnO_2$ is seen (Figure 11). As for the EDXRD experiments, the reactions were modeled using the Avrami−Erofe'ev model. Extent of reaction plots are included in Figure 12(a) and Sharp−Hancock plots in Figure 12(b). The kinetic parameters calculated are summarized in Table 2.

The values of *n* lie between 0.5 and 1.5, which is consistent with a mechanism that involves 1D diffusion control fol-

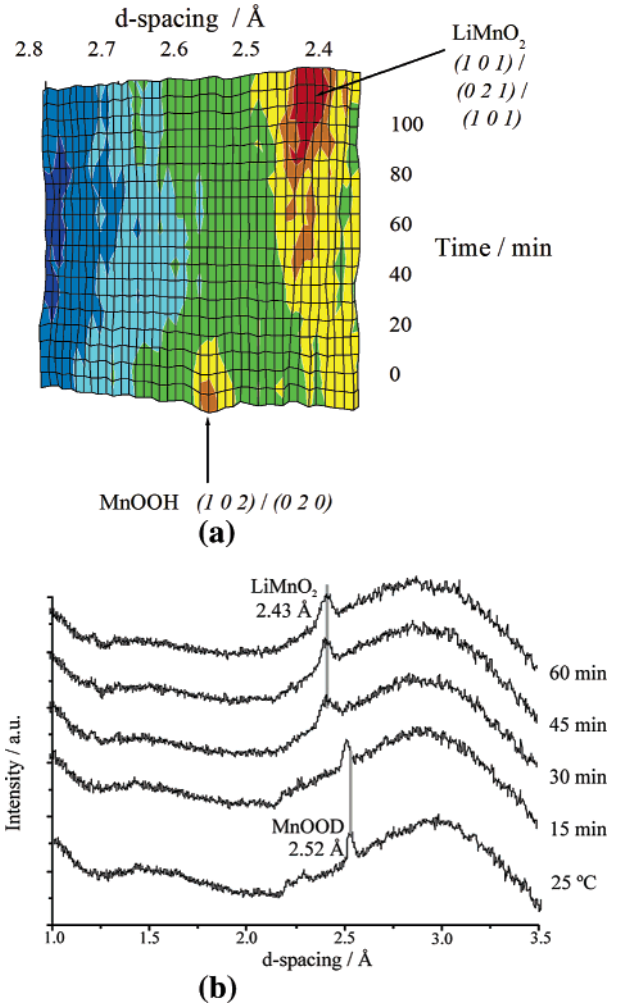

Figure 10. ND data for the reaction at 100 °C: **(a)** 3D stacked plot and **(b)** 2D stacked plots showing data collected at room temperature and then at various time periods after the desired reaction temperature was reached. Reflections corresponding to both the starting material and product are visible; the small difference in *d* spacing between these means they can only be resolved by ND.

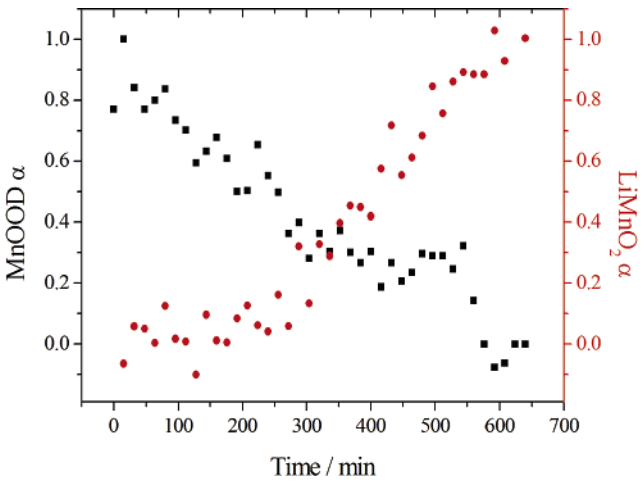

Figure 11. Extent of reaction area vs time for the in situ ND experiment at 80 °C. The first data point shown is the first scan recorded after the reaction temperature was reached.

lowing deceleratory nucleation. Although similar to the mechanism deduced from the EDXRD data, there are subtle differences which will be discussed below. Use of the Arrhenius equation (Figure 13) allows an estimate of 150.2 ± 3.2 kJ mol^{-1} to be made for the activation energy. Again, there is significant deviation from the EDXRD data here.

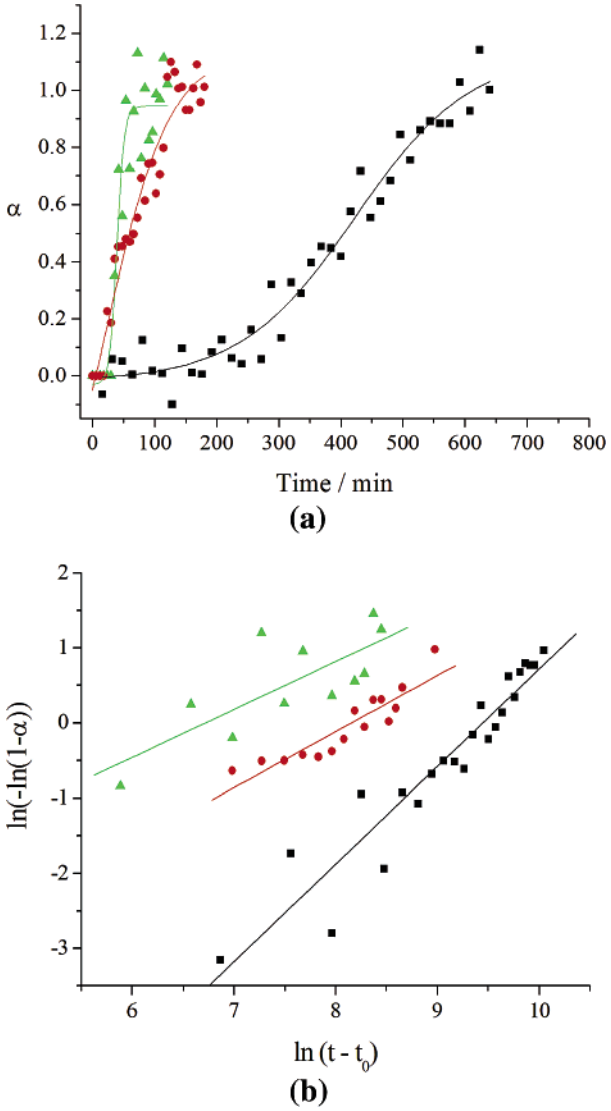

Figure 12. **(a)** Extent of reaction vs time plot for the reaction between LiOD and MnOOD at 80 (black squares), 90 (red circles), and 100 (green triangles) °C. **(b)** Sharp−Hancock plots at the same temperatures. The first data point shown in each case is the first scan recorded after the reaction temperature was reached.

Table 2. Kinetic Parameters for the Formation of $LiMnO_2$ from MnOOD and LiOD, Calculated from ND Data

T/°C	*n*	$k/(10^{-4}\ s^{-1})$	$t_{0.5}$/s
80	1.30 ± 0.09	0.79 ± 0.08	24480
90	0.80 ± 0.07	3.04 ± 0.25	3780
100	0.64 ± 0.18	12.07 ± 0.73	2400

Discussion

It has been established that the reaction between LiOH and MnOOH (or their deuterated analogues) proceeds directly from the starting materials to the product using in situ techniques. No intermediates are observed, and the crossing of the extent of reaction vs time curves at 0.5 suggests that no intermediates, neither crystalline nor amorphous, exist. At 100 °C, the reaction is complete in ca. 90 min; at 130 °C this time is reduced to approximately 30 min.

There are some distinct differences observed between the EDXRD and ND data. First, the activation energy is greater

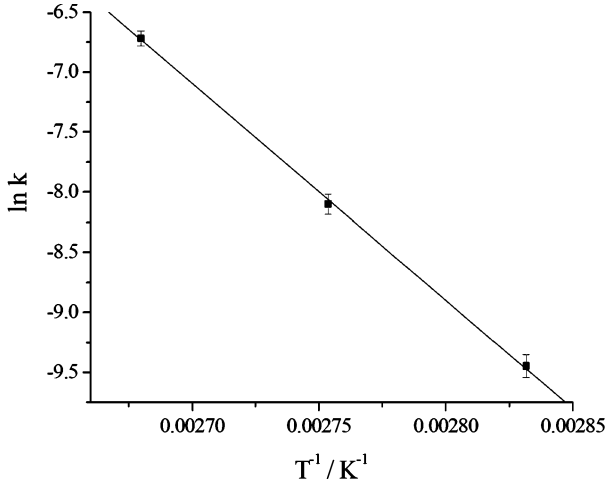

Figure 13. Arrhenius plot for the reaction between MnOOD and LiOD.

in the ND experiments (by ca. 69 kJ mol^{-1}). This fairly large difference results from differences in the zero-point energies of the O−D and O−H bonds. The first step in the reaction involves the deprotonation of a OH (OD) group, which is more facile for OH than OD because of the higher vibrational energy of the OH group in the $v = 0$ level. This is a manifestation of the kinetic isotope effect. A requirement of multiple deprotonations for the reaction to begin will account for the large difference in E_a. At 100 °C, the ratio $k_H/k_D \approx 0.6$. This might reflect the fact that, following deprotonation, D_2O and H_2O are formed. The O−H(D) bond in water will be stronger than that in MnOOH(D) owing to the electron-withdrawing nature of Mn^{3+}, which weakens the O−H(D) bond and labilizes the group to ionization. Therefore, stronger bonds than those existing prior to reaction are formed in the transition state. However, since there is only a single value to consider, this postulation must be treated with caution, particularly given that the two rates are very similar when experimental error is taken into account.

The probability of a single site reacting at any moment in time will be the same, *p*. There are a given number of nucleation sites (shared vertexes), *x*, at the start of the reaction, so the probability of a site reacting is *px* initially. As the reaction proceeds, some of the nucleation sites, *y*, become consumed. Therefore, after time *t*, the probability of a nucleation site reacting is $p(x - y)$. That is, the likelihood of a nucleation site reacting declines with time: deceleratory nucleation.

Once one linkage has sheared, strain will be introduced into the structure and the splitting of the 3D structure into layers will be propagated around this initial site (Figure 8). Therefore, the condensation of some chains together to form a layer will encourage layer formation in the third dimension. The reaction mechanism in the protic case is more likely to be 1D phase boundary control following deceleratory nucleation. The breaking of the vertex links cannot happen by a diffusion process: instead, some activation event is required to cause this fission. The propagation of the newly formed layers in the *b* direction (perpendicular to the layers) is observed experimentally. It is proposed that the reaction begins by the deprotonation of a OH group in the MnOOH material. This produces an "O^-" group, and electrostatic repulsions cause the breakage of a vertex link between two chains. To preserve local electroneutrality, it is probable that the Li^+ cations diffuse into the structure as soon as each breakage occurs.

A slightly different mechanism is observed in the ND experiments. Both the EDXRD and ND processes involve deceleratory nucleation, but the former is followed by 1D phase boundary control, whereas the latter is followed by 1D diffusion control. It is believed that the 1D process observed following nucleation is the 1D propagation of the layers in the *b* direction. The mechanistic differences therefore suggest that it is more facile for the chains to condense into layers in the deuterated material, a result of the kinetic isotope effect discussed above. In the protic system, removal of a proton(s) to begin the reaction is a relatively-low-energy process, so this happens rapidly. The rate of condensation of the layers is comparable to this, and hence, phase boundary control is observed. In contrast, in the deuterated system, loss of D^+ to begin the reaction is much more difficult. As soon as sufficient ionization has occurred for the chains to begin to condense, they do so very rapidly, and thus, diffusion control is seen following nucleation.

Summary

An in situ X-ray and neutron diffraction study into the formation of the potentially important battery material $LiMnO_2$ has been conducted, in which a one-step conversion is observed. Differences in reaction activation energies and nucleation mechanisms between the MnOOH and MnOOD reactions result from the differences in the O−H and O−D bond energies. A reaction mechanism is proposed that is supported by both the EDXRD and ND experiments.

Acknowledgment. We thank the EPSRC for funding and the CCLRC for access to the U.K. SRS and ISIS facilities. Dr. Dave Taylor and Mr. Alfie Neild (SRS) and Dr. Ron Smith, Dr. Lauren Chapon, and Prof. Alex Hannon (ISIS) are also gratefully acknowledged for their expertise and assistance.

CM0611791